

Transport properties of individual C₆₀-molecules

G. Géranton,¹ C. Seiler,^{1,2,3} A. Bagrets,^{1,4} L. Venkataraman,⁵ and F. Evers^{1,2,3}

¹ *Institute of Nanotechnology, Karlsruhe Institute of Technology, Campus North, D-76344 Karlsruhe, Germany*

² *Center of Functional Nanostructures, Karlsruhe Institute of Technology, Campus South, D-76131 Karlsruhe, Germany*

³ *Institut für Theorie der Kondensierten Materie,*

Karlsruhe Institute of Technology, Campus South, D-76128 Karlsruhe, Germany

⁴ *Steinbuch Center for Supercomputing, Karlsruhe Institute of Technology, D-76344 Karlsruhe, Germany*

⁵ *Department of Applied Physics and Applied Mathematics, Columbia University, New York, NY 10027*

(Dated: October 21, 2021)

Electrical and thermal transport properties of C₆₀ molecules are investigated with density-functional-theory based calculations. These calculations suggest that the optimum contact geometry for an electrode terminated with a single-Au atom is through binding to one or two C-atoms of C₆₀ with a tendency to promote the sp²-hybridization into an sp³-type one. Transport in these junctions is primarily through an unoccupied molecular orbital that is partly hybridized with the Au, which results in splitting the degeneracy of the lowest unoccupied molecular orbital triplet. The transmission through these junctions, however, cannot be modeled by a single Lorentzian resonance, as our results show evidence of quantum interference between an occupied and an unoccupied orbital. The interference results in a suppression of conductance around the Fermi energy. Our numerical findings are readily analyzed analytically within a simple two-level model.

PACS numbers: 73.63.Rt, 73.63.-b, 73.23.Ad

I. INTRODUCTION.

C₆₀ on metal surfaces is an important model system for understanding basic processes in binding of (conjugated) organic molecules to metal electrodes, and has been studied in the past both experimentally and theoretically.¹⁻⁸ Transport through C₆₀ has motivated investigations by experimentalists and theorists from early on with an emphasis on correlation physics like the Kondo effect⁹⁻¹³ or vibrational degrees of freedom¹⁴⁻¹⁸.

Concerning the linear conductance, the situation seems to be particularly well investigated with Cu-electrodes, where a combination of ab-initio based calculations and STM-experiments have provided a detailed understanding.¹⁹⁻²¹ These investigations suggest that the conductance, G , of C₆₀ bound to Cu(111)-substrates is sensitive to the anchoring mechanism. In general, G is relatively large for a single Cu-atom contacting C₆₀ immobilized on a Cu(111) surface ($\sim 0.13 G_0$, where $G_0 = 2e^2/h$).²² In contrast, the conductance of C₆₀ on Au-electrodes has not been studied extensively. Mechanical break junction experiments have found that the conductance of a junction can be as high as 0.1 – 0.2 G_0 ^{23,24} while STM-break junction experiments report much smaller values with a very broad scattering in conductance histograms for Au-, Pt- and Ag-electrodes²⁵.

Understanding the transport mechanism in C₆₀/Au junctions is of interest for two reasons. First, any analysis and design of transport processes through single molecules relies upon an understanding of the influence of the electrodes.²⁶ Second, the specific molecule C₆₀-molecule might play a special role in the context of contact formation because it was recently proposed to be a suitable general anchor group due to its size and electronic conjugation.^{27,28}

In this paper we address the transport characteristics of single-molecule junctions formed using C₆₀ molecules attached to Au electrodes. Our calculations are employing the DFT-based non-equilibrium Green's functions (NEGF) formalism²⁹. Our first theoretical result is that Au-electrodes are invasive: Au single adatoms have a tendency to form chemical bonds with C-atoms and thus locally affect the sp²-conjugation in C₆₀, similar to what has been reported for Cu electrodes. We find that the alternative scenario, where the adatom resides in a hexagonal/pentagonal facet of C₆₀ is not energetically favored as it has a binding energy that is 0.5eV lower. We thus confirm statements reported in Ref. 30. Our second result is that C₆₀ has a slight tendency to charge negatively on Au with single adatom binding, though not as much as on Cu (or Ag).³¹ This contrasts results on flat Au(111) where the charge transfer is negligible.^{4,5} As a consequence, with Au-electrodes transport is more LUMO-dominated. However, in contrast with Cu, it will in general not be close to resonant. Third, we determine the transport characteristics of several C₆₀-junctions that exhibit somewhat different contact geometries by calculating the transmission function, $T(E)$, and the Seebeck-coefficients, $S(E)$. For two geometries data similar to ours have been reported before³². Our analysis goes significantly beyond earlier work because we provide evidence that interference between transport channels plays a quantitatively important role, especially when the Fermi-energy is situated between HOMO- and LUMO-resonances of the C₆₀ molecule. We show that deviating from earlier claims³³ the conductance at the Fermi energy is not resonant but rather strongly suppressed due to destructive interference from two strongly coupled transport channels. This suppression leads to a sharp, step-like increase of the Seebeck-coefficient near

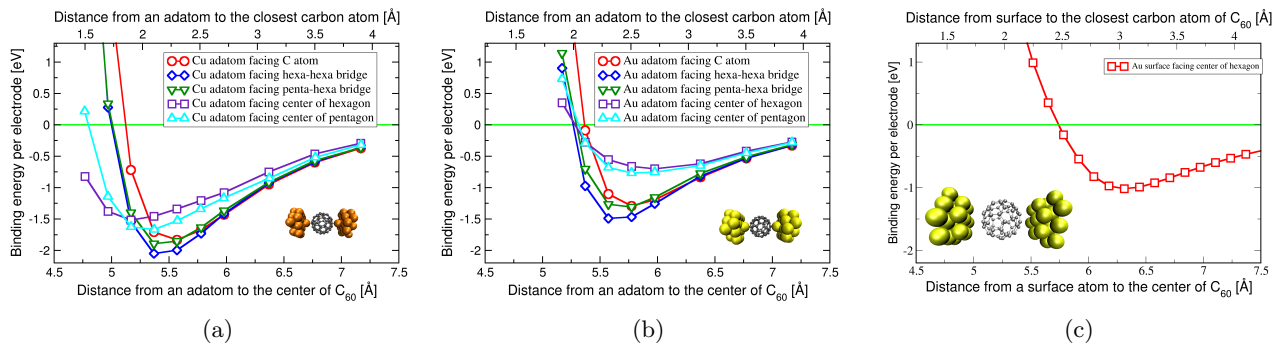


FIG. 1: Energy profiles from DFT with Grimme corrections: Adatom geometries with Cu-electrodes (a) and Au-electrodes (b). (c): Flat Au-electrodes facing C_{60} hexagons.

the minimum transmission energy. We analyze our findings within an analytic model for a two-level system and find that it supports the results of DFT-based transport calculations. In addition, this analysis also shows that due to cancellation effects, electrical currents driven by heat gradients (rather than by a bias voltage) remain almost unaffected by destructive interference effects.

II. SYMMETRIC CONTACTS WITH SINGLE ADATOM

A. Method

We compute the total energy of the extended molecule (C_{60} plus contact model) for different contact geometries using density functional theory (DFT). To this end, we employ the TURBOMOLE package³⁴ with the BP86 functional³⁵ and van der Waals interactions included on the level of Grimme corrections³⁶; see appendix A for details on them. The geometry was optimized in the following way: the relative position of all electrode atoms was fixed with bond-lengths as given by Au-bulk. The geometry of C_{60} was optimized in vacuum. Thereafter, C_{60} was approached to the electrode with different surface-molecule contact geometries: hexagon or pentagon on the flat surface or atop (C-Au-atom) and bridge position for single-adatom geometries, see Fig. I. For each contact geometry a trace binding-energy was recorded as a function of distance. In this process the geometry of C_{60} was fixed.

B. Results: Adatom geometries

Binding energies for different inter-electrode distances are displayed in Fig. I. One infers from Fig. Ia,b that Cu or Au-adatoms prefer bonding in bridge positions, where two hexagons touch each other (*hexa-hexa-bridges*). However, for larger distances between the electrodes, i.e. more generally for relaxation under external

constraints, adatoms may also sit on-top of C-atoms or in *penta-hexa* bridge position. Since the energy difference between these three geometries is under 100 meV even close to the minima, these three geometries should be energetically accessible, especially in break-junction experiments where the electrode structures can deviate from pyramidal tips.

Discussion: Carbon atoms of C_{60} in vacuum are sp^2 -hybridized. However, the bond angle (108°) is relatively far from the “ideal” sp^2 -hybridization value ($\approx 120^\circ$). Therefore, it is plausible that C_{60} is susceptible for bonding with adatoms³⁷, in contrast to simple sp^2 -hybridized carbon like graphene or other conjugate molecules. Fig. Ia,b reveal that the binding energy of Cu to C_{60} exceeds that of Au by 0.5eV. On a qualitative level this observation could be related to the fact that the KS-work function of Cu is situated considerably above the one of C_{60} in vacuum (see Fig. 2). Therefore, a moderate flow of electrons into the C_{60} -LUMO might increase the interaction with the Cu-surface as compared to the one of Au.

The relatively strong interaction between the carbon π -system and the Au-adatom also manifests itself in the ratio of the GGA binding energy (ignoring Grimme the corrections) to the total binding energy, $\rho \equiv E_{GGA}/(E_{GGA} + E_{Grimme})$. It helps to quantify how close the bond is to being covalent. If $\rho \approx 1$, the van der Waals contribution is negligible and a covalent chemical bond has formed. In contrast, if $\rho \ll 1$, bonding is predominantly of the van der Waals type and the adatom should be thought about as being physisorbed.

The ratios ρ are given in Table I along with the corresponding total binding energies and bond lengths. For both Cu and Au-electrodes, the values $\rho \geq 1/2$ suggest that bonding is predominantly covalent consistent with the expectations formulated in the preceding paragraph.

Electrode	Position	l_{bond} [Å]	E_{bind} [eV]	ρ
Cu	C-atom	2.0	-1.83	66%
	p-h bridge	2.2	-1.89	61%
	h-h bridge	2.2	-2.05	63%
Au	C-atom	2.2	-1.29	56%
	p-h bridge	2.4	-1.31	54%
	h-h bridge	2.2	-1.49	54%
Au (flat)	hexagon	3.0	-1.02	-32%

TABLE I: Characteristics of lowest energy molecular junction geometries where l_{bond} is the Au-C or Cu-C bond length, E_{bind} the binding energy per electrode and $\rho \equiv E_{\text{GGA}}/E_{\text{bind}}$ gives an indication of the covalent contribution to the bond.

C. Results: Flat Au(111) electrodes

We also consider flat Au(111) electrodes (without an adatom) facing a hexagon of C_{60} . The binding energy profile of that configuration is displayed in Fig. 1c. The bond distance here is measured from the position of the nuclei of the first Au(111) layer. Most notably, the pure GGA functional without Grimme corrections would indicate that the configuration at a distance of ~ 3.0 Å is non-binding. This is reflected in the sign of ρ in Table I. The bond has no covalent contribution in this geometry, consistent with the higher coordination number of surface atoms compared to adatoms. As shown in Table I, the bond distances for the C_{60} -Au(111) geometry is $0.8 - 1.0$ Å larger than in the case of C_{60} -adatom geometry. The binding energy is of similar magnitude as in the adatom case, indicating that this configuration may indeed be relevant in experiments.

III. ELECTRONIC STRUCTURE

The nature of the molecule-electrode bond is of crucial importance for C_{60} transport properties. Since the formation of a covalent bond with C_{60} implies that the conjugation of the π -electron system is broken at the contact, a transport barrier forms and the molecule should be considered as “weakly coupled”. In this section we discuss the effect of the bonding on the electronic structure of the molecule.

A. Free molecule

The position of relevant molecular orbitals of C_{60} in vacuum, as obtained from DFT calculations, is shown in Fig. 2. The Highest Occupied Molecular Orbital (HOMO) and Lowest Unoccupied Molecular Orbital (LUMO) levels are 5-fold and 3-fold degenerate. The associated HOMO-LUMO gap is $\Delta \sim 1.6$ eV, slightly underestimating the experimental value 2.3 eV³⁸. (For

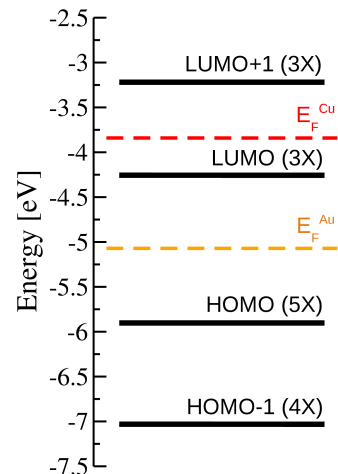


FIG. 2: Kohn-Sham energy levels of C_{60} in vacuum (black lines). Fermi energies of Cu (red) and Au (yellow) estimated from DFT calculation for the 24-atoms clusters used for the transport calculations.

a discussion of this discrepancy, see Sec. IV E.) The position of the chemical potentials of Au and Cu relative to C_{60} energy levels are also shown in Fig. 2. These values are from DFT calculations on 24-atoms clusters since the same values will be used in our transport calculations. The position of these levels suggest that charge transfer between the Au-electrode and molecule will be relatively weak, in comparison with Cu-electrodes where the molecule can pick up a pronounced negative excess charge.

B. Local Density of States

When the molecule is in contact with metal electrodes, the position of these molecular levels will shift and experience a lifetime broadening. The electronic structure of the junction is represented by the density of states projected on the C_{60} (local density of states, LDOS). We calculate it for the geometries of lowest total energy with the DFT-based Green’s function formalism for non-interacting particles described in Appendix B and Ref. 29. The result is displayed in Fig. 3a,b.

To quantify further, we parametrize the LDOS as a sum of Lorentzians,

$$\text{LDOS}(E) = \frac{1}{\pi} \sum_n \frac{\delta_n}{(E - \epsilon_n)^2 + \delta_n^2}. \quad (1)$$

Values of the fitting parameters, resonance position ϵ_n and broadening δ_n , are given in Table II for junctions where the adatom is facing a C-atom of the C_{60} (Fig. I).

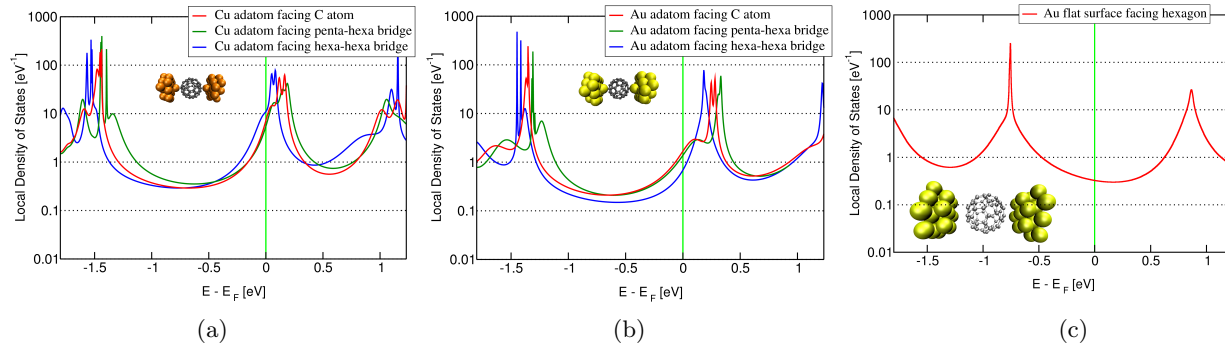


FIG. 3: (Color) Local Density of States (LDoS) projected on C_{60} for Cu-electrodes (a) and Au-electrodes (b) for the three geometries of lowest total energies identified in Fig. 1. (c) LDoS of C_{60} in a junction with direct coupling to a flat Au(111) surface for the optimum geometry, see Fig. 1c.

		HOMO					LUMO			LUMO+1		
		Au	$\epsilon_n - E_F$ (eV)	-1.68	-1.38	-1.37	-1.35	-1.35	0.10	0.25	0.28	1.15
	δ_n (meV)	149	26	8	1	6	116	8	6	175	21	1
Cu	$\epsilon_n - E_F$ (eV)	-1.59	-1.48	-1.48	-1.45	-1.44	0.06	0.12	0.16	1.02	1.15	1.24
	δ_n (meV)	55	15	17	5	3.5	50	12	11	60	40	1.1
Au (flat)	$\epsilon_n - E_F$ (eV)	-0.78	-0.77	-0.76	-0.75	-0.75	0.84	0.86	0.87	1.92	1.92	1.93
	δ_n (meV)	114	116	4	2	2	82	75	17	9	42	53

TABLE II: Linewidths, δ_n , and positions of energy levels, ϵ_n , for the geometry where the adatom sits on-top of a C-atom, and the flat surface geometry. Levels are classified according to their position in the energy spectrum of the molecule in vacuum (HOMO, LUMO, HOMO+1).

1. Adatom geometry

The splitting of molecular energy levels in Fig. 3, especially the LUMO ones, indicates that the formation of the chemical bond constitutes a significant perturbation in the sense that one of the LUMO states of the molecule splits away from the others. It hybridizes more strongly with the electrode states as exhibited by the corresponding increased level broadening. Electron transport through C_{60} will be mostly via this level. Table II reveals the effect of electrode coupling on level splitting and broadening is about two times stronger for Au- than for Cu-electrodes.

2. Flat Au(111) contacts

With a flat Au(111) surface (see Fig. 1c) E_{Fermi} resides in the middle of the HOMO-LUMO gap, much closer to its vacuum position (see Fig. 2) than in the adatom geometries. This indicates, that partial charge transfer is weaker with a flat electrode as compared to the case of adatoms, reflecting that binding is purely of the van-der-Waals type. Consequently, the splitting of the energy levels (see Table II) is much smaller than that of the adatom

geometry. In other words, the presence of the electrodes implies only a weak symmetry breaking with an overall small effect on the molecular frontier orbitals. We associate the large quantitative differences in the observed shifts and broadenings with wavefunction overlaps: symmetry related extinction results in reduced hybridization matrix elements.

IV. TRANSPORT CALCULATIONS FOR C_{60}

If we were to consider a system with N channels that do not interfere with each other, then by definition the transmission (per spin) could be written as a sum of Lorentzians,

$$T(E) = \sum_n \frac{\delta_n^2}{(E - \epsilon_n)^2 + \delta_n^2}. \quad (2)$$

with parameters given in Table II. The formula yields a good approximation, usually, in the presence of symmetric coupling if a single transport resonance dominates. However, in cases where transfer amplitudes of different channels can be of comparable magnitude interference terms may become significant and the approximation (2)

breaks down. Then, in principle, the Landauer formula, Eq. (B4) in the appendix, has to be employed.

A. Results: Transmission function

The full transmission function, $T(E)$, as obtained from the Landauer formula in the NEGF-formulation²⁹ is displayed in Fig. 4a,b for the Au-C atop-geometry. It exhibits pronounced non-Lorentzian features, with a suppression of the transmission in the valley region. Comparing with the model of isolated resonances, Eq. (2), one can see that the missing cross-terms between different transfer modes explains this behavior. We conclude that interference between transport resonances play a quantitatively important role in electron transport through C₆₀ when the chemisorbed C₆₀-molecule is only weakly charged. The conductance could be reduced by roughly one order of magnitude as a result

B. Discussion: effective two level model

We interpret our findings for the transmission function using an effective two level model. Its precise definition together with a derivation of basic properties are given in the appendix D.⁵⁶ The salient feature of the simplified model are summarized by the following set of equations:

$$T(E) = T_0 + T_1 \pm \bar{T}_{01} \quad (3)$$

$$\bar{T}_{01}(E) \approx 2\sqrt{T_0 T_1} \frac{(E - \epsilon_0)(E - \epsilon_1) + \gamma_0 \gamma_1}{\sqrt{(E - \epsilon_0)^2 + \gamma_0^2} \sqrt{(E - \epsilon_1)^2 + \gamma_1^2}} \quad (4)$$

The two levels that one should refer to here derive from the C₆₀-HOMO quintett and LUMO-triplett, that exhibit resonances with the strongest broadening. Accordingly, we see from Table II the set of parameters: $\epsilon_0 = -1.68\text{eV}$, $\epsilon_1 = 0.1\text{eV}$, $\gamma_0 = 0.149\text{meV}$, $\gamma_1 = 0.116\text{meV}$. A decomposition of the LDoS given in Appendix C further substantiates this simplification.

The sign in Eq. (3) controls the effective mixing between the two transport channels, i.e. whether they interfere constructively (minus sign) or destructively (plus sign) energies in the valley region, $\epsilon_0 < E < \epsilon_1$. As we explain in the appendix, destructive interference occurs in two-level models where both states couple with similar strength to both reservoirs. For C₆₀, we expect that there should not be any important difference between the coupling of the HOMO and LUMO levels to the leads, we can expect to see destructive interference.

Indeed, already from Fig. 4 we can see that for the case of the C₆₀-Au-junction, the transmission in the valley region is very strongly suppressed supporting our claim.

Hence, we conclude that the plus-sign should be chosen in Eq. (3). Furthermore, with symmetric coupling we also have

$$T_i(E) = \frac{\gamma_i^2}{(E - \epsilon_i)^2 + \gamma_i^2}, \quad i = 0, 1. \quad (5)$$

The sign in Eq. (3) is the toy model's only ingredient in $T(E)$ that is not fixed by the LDOS alone.

In Fig. 5 (left) we compare the full transmission with the one from the toy model, Eq. (3). Indeed, in the valley region the toy model reproduces the transmission and all its non-Lorentzian features well up to a small shift of the minimum-transmission energy. This shift is readily explained, e.g., by residual energy dependencies in the pole-positions due to the structured density of states in the reservoirs. For the minimum conductance at energy ϵ^* we obtain a parametrical estimate $T_{\text{constr}}^* \approx 4\gamma_0\gamma_1/|\epsilon_0 - \epsilon^*||\epsilon_1 - \epsilon^*|$ for constructive interference and

$$T_{\text{destr}}^* \approx \frac{1}{4} T_{\text{constr}}^{*2} \quad (6)$$

in the other case.

C. Thermopower

We complete our account of C₆₀ transport properties with a discussion of the thermopower of an Au-C₆₀-Au junction. The thermopower or Seebeck coefficient S determines the magnitude of the built-in potential developed across the junction when a temperature difference $\Delta\mathfrak{T}$ is applied.³⁹ In particular, molecular junction thermopower can be useful in determining the dominant molecular orbital for transport and the identity of the primary charge carriers.^{40,41} With the additional presence of an external voltage bias ΔV across the junction^{42,43}, the total current I in this case is simply

$$I = \frac{2e^2}{h} [-T(E_F)\Delta V + T(E_F)S(E_F)\Delta\mathfrak{T}] \quad (7)$$

where $T(E_F)$ denotes the transmission at the Fermi energy. For non-interacting electrons, the Seebeck-coefficient, $S(E)$, is closely related to the transmission function $T(E)$, ultimately, because all transport processes are controlled by the tunneling probabilities of electrons with a given energy through the barrier. We have (using the convention $e = |e|$)

$$S(E) = \frac{\pi^2 k_B^2 \mathfrak{T}}{3e} \frac{d \ln T(E)}{dE} \quad (8)$$

where \mathfrak{T} denotes the (electronic) temperature. The system specific information is all encoded in the logarithmic derivative, which we now discuss.

Fig. 5b displays the logarithmic derivative for our model system, C₆₀. Again, we can convince ourselves that the two-level model with destructive interference accounts well for the salient features of the full DFT-based trace. A striking characteristics to be observed here is the step-like transition, changing sign, that the derivative undergoes when the energy sweeps by the valley minimum point $\epsilon^* \approx -0.51\text{eV}$. We can estimate the parametrical

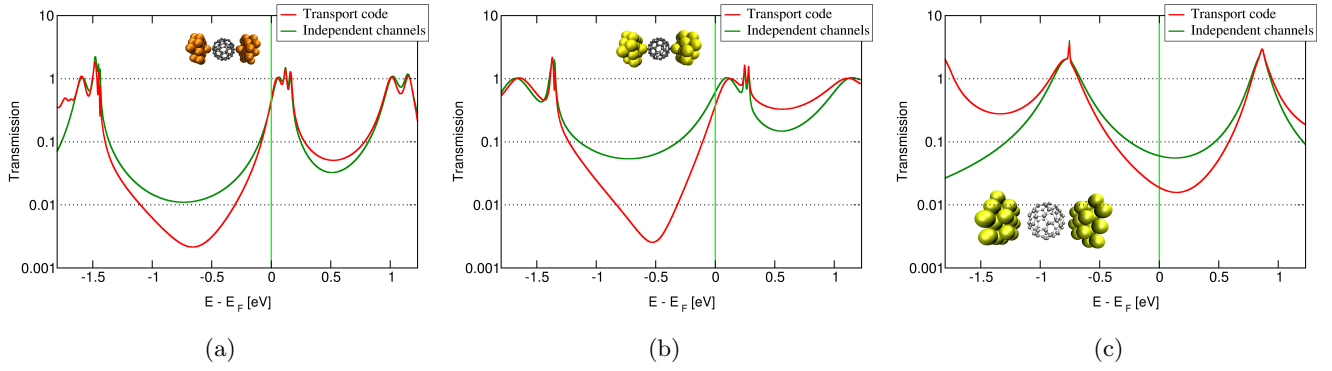


FIG. 4: (Color) Transmission functions for different electrode models. Adatom in atop-position with Cu-electrode (a), and Au-electrode (b). (c) displays the flat Au(111)-surface. Red line: DFT-based transport code with Landauer formula/NEGF-formalism. Green line: isolated resonances model, Eq. (2). Plot highlights the effect of crosstalk between different transport channels in the transmission valley regime of energies.

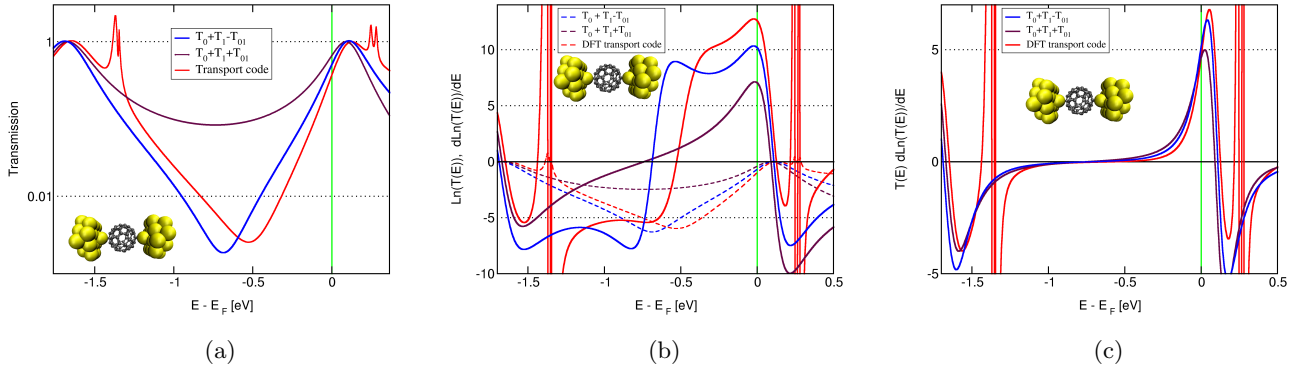


FIG. 5: (Color) (a) Comparison of transmissions obtained from the transport code (Fig. 4(b), solid red) and the two-states model (solid blue), see Eq. (3). In order to highlight the impact of the interference term, \bar{T}_{01} , Eq. (3), results for constructive and destructive situations are given. (b) Logarithm of the transmission function (dashed lines) and its derivative. The latter represents the system specific information content of the Seebeck-coefficient, Eq. (8). (c) System specific, energy dependent characteristics, $T(E)d \ln T(E)/dE$, of the thermal current Eq. (7). Plot highlights a result of the two-level model: traces for destructive (blue) and constructive (brown) interference give nearly coinciding results, even though their electronic transmission deviates by orders of magnitude, see the transmission functions given in the left figure.

dependency of the slope at ϵ^* employing Eqs. (3-5):

$$\left. \frac{d \ln T(E)}{dE} \right|_{E \approx \epsilon^*} \approx \frac{(E - \epsilon^*)(\epsilon_1 - \epsilon_0)^2}{2\gamma_0\gamma_1|\Delta_0\Delta_1|}, \quad |E - \epsilon^*| \lesssim \gamma_0, \gamma_1 \quad (9)$$

where $\Delta_i = \epsilon_i - \epsilon^*$. For the typical cases where γ_0 and γ_1 are comparable, ϵ^* is halfway between ϵ_1 and ϵ_0 , so the expression simplifies further: $d \ln T(E)/dE|_{\epsilon^*} \approx 2(E - \epsilon^*)/\gamma_0\gamma_1$. Hence, the slope diverges in the weak coupling limit, where $\gamma_{0,1}$ tend to zero at fixed level splitting $|\epsilon_1 - \epsilon_0|$.

The estimate for the slope is valid for energies in a vicinity of width $\gamma_{0,1}$ about ϵ^* . Hence, the logarithmic derivative takes very large magnitudes $\sim \pm 1/\gamma_{0,1}$ near the center of the valley region. It is only near the resonances where it reaches similar values, e.g. $\sim 1/\gamma_1$ near ϵ_1 . The intermediate region interpolates between these to maxima.

This behavior is typical of systems that exhibit almost perfect destructive interference, so that $T(E)$ approaches zero near some energy ϵ^* . It is completely absent with constructive interference, see Fig. 5 (center). There the logarithmic derivative has a parametrically small slope of the order of $\sim 1/|\Delta_0\Delta_1|$ (rather than $1/\gamma_0\gamma_1$) near ϵ^* .

The temperature driven current is, up to system un-specific prefactors, given by the product $T d \ln(T)/dE$. Each factor has been seen to be very sensitive to the sign in Eq. (3) in our discussion. For the product this is not the case, as one infers from Fig. 5c. The reason is that the suppression of T^* for the case of destructive interference is largely compensated by the strong slope in the logarithmic derivative. Indeed, in the valley region we have for the product with either destructive or constructive interference a similar behavior: $T^* d \ln(T)/dE \approx (\epsilon - \epsilon^*)\gamma^2/\delta^4$, where $\gamma = \gamma_0 = \gamma_1, \delta =$

$\Delta_0 = -\Delta_1 = (\epsilon_0 - \epsilon_1)/2$ has been assumed.

Hence, we arrive at the following conclusion: In the presence of destructive interference (minus sign in Eq. (3)) the bias voltage driven current can be suppressed by orders of magnitude in the valley region. Nevertheless, an electrical current driven by a thermal bias reaches similar values as it would in the absence of interference effects.

D. Contact geometries revisited: asymmetry and chain formation

In this section we show, that the shape of the transmission function can be significantly modified by changing the contact geometry.

1. Single adatom contacts breaking inversion symmetry

By selecting different pairs of C-atoms on the molecule, one modifies the phase difference between parallel transmission paths (Fig. 6). The situation is similar to the case considered perviously^{44,45}, except that there a torus geometry was considered while we investigate a sphere. The different contact geometry has an impact on the effect of T_{01} . Specifically, the transmission function for the second geometry (maroon trace in Fig. 6) is very similar to a pure superposition of Lorentzian resonances, suggesting that the T_{01} in Eq. 3 does not contribute significantly and interference effects between parallel paths are much weaker than in the other cases.

In contrast, destructive interference reappears in geometry (3), Fig. 6. This geometry is however, far from perfectly symmetric, and therefore the simplified model Eq. (4) cannot be expected to hold. Instead, in principle the more complete formula given in the appendix, (D13-D15), should be applied. Indeed, the fit based on the simplified expression (3) does not properly reproduce the behavior of $T(E)$ in the valley region. (Based on the discrepancy one expects $\cos(\Psi_c) \approx -0.8$.)

We emphasize that there is a very large variability of the conductance in the valley region even though all electrode positions (1-3) are associated with similar resonance positions and broadenings. We attribute this behaviour to the mixing angle Ψ_c oscillating from π (geometry 1) to 0 (2) back to larger values $\Psi_c \approx 2.5$ (3) again. This observation we take as support for our claim that the variations observed in the transmission function are due to a modification of the phase difference between parallel paths.

2. Au-contact chains

In order to investigate the development of interference with decreasing level broadening, we consider here geometries where the molecule is included between Au-

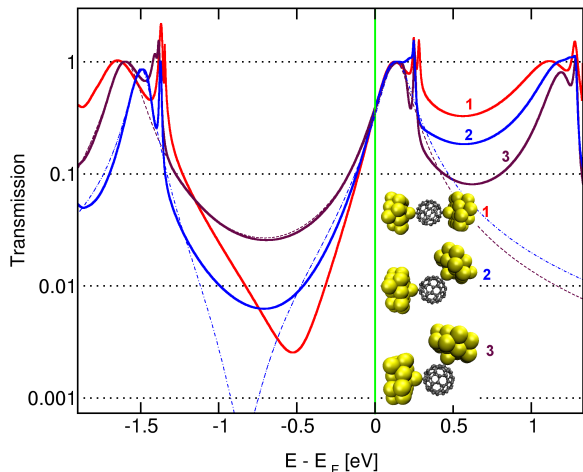


FIG. 6: Transmission function for different anchoring geometries: (1) Symmetrical geometry from previous plot Fig. 5. Asymmetrical geometries (2, maroon; 3, blue). Position (2) can be fitted by adding two Lorentzians (dashed line, $\gamma_0 = 0.106$, $\epsilon_0 = -1.6$, $\gamma_1 = 0.096$, $\epsilon_1 = 0.13$), indicating that interference effects are weak. In contrast, geometry (3) exhibits destructive interference. The model (3) fails in the valley region (blue dot dashed line), mainly because the angle Ψ_c (defined in Appendix D) is not close to π . From the blue data trace one estimates roughly $\cos \Psi_c \approx -0.8$ together with an asymmetry $\gamma_{0L}/\gamma_{0R} \approx 0.45$.

chains. In this configuration, the number of incoming and outgoing lead channels is limited to essentially a single one. This reflects in the local density of states at the chain terminating Au-atom that the molecule couples to. It is more strongly structured as compared to the case with a single Au-adatom, only; the number of states that are ready to hybridize with the C_{60} -orbitals is reduced. As a consequence, broadening of molecular orbitals contacting Au-chains is in general weaker, and also more complicated since a convolution of two structured functions (LDoS on molecule and contact-atom/Au-wire) is involved.

The transmission functions obtained for one, two and three-atoms chains geometries shown in Fig. 7 support these expectations. We observe a progressive development of large amplitude anti-resonances with increasing chains length. They reflect the fact molecular states and wire states can cooperate in a complicated manner which allows, in particular, for more levels to develop interference patterns in valley regions. In this way, transmission values below 10^{-4} can come about for 3-atoms chains, which suggests that extremely low conductance values, between $10^{-3}G_0$ and $10^{-4}G_0$, see Fig. 7, can be observed with this type of junctions. This finding becomes particularly interesting in view of the fact, that a single Au-chain is well known to exhibit a single perfectly transmitting channel. Our result Fig. 7 gives a solid demonstration, that due to quantum effects even a per-

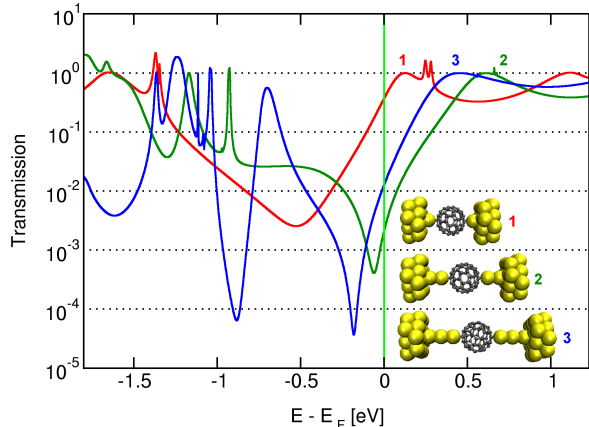


FIG. 7: Transmission functions for contacts made via adatoms (1), two-atoms Au-chains (2) and three-atoms Au-chains (3).

fect conductor can be a very invasive means to facilitate an electrode coupling.

E. Additional remarks

We add several remarks on artifacts of DFT-based transport calculations and about experiments.

First, the functionals used in our study are well known to underestimate the true HOMO-LUMO gap, as was pointed out already in section III A. The missing derivative discontinuity influences the alignment of the molecule-based and metal-based electronic levels; in general it leads to an overestimation of charge transfer. Hence, while one expects that the qualitative features of the DFT-based transport calculations are captured correctly, the positioning of the LUMO with respect to the Fermi-energy, E_F , should be slightly too close. The true E_F is probably situated somewhat closer to the valley region than seen in the DFT-calculation.

Second, recent research has shown that DFT-based transport calculations employing exact functionals reproduce the exact transmission for interacting *single* level models.^{46–48} At present, a rigorous generalization of the statement to models with several levels does not exist. In contrast, the numerical results of Ref.⁴⁹ show deviations between exact conductances and DFT-based transport with exact functionals in the valley region indicating that a precise generalization to two-level models may in fact not exist.

In view of this problem, it is important to realize that the main finding of our paper is likely to be insensitive to (weak) interaction effects beyond our GGA treatment. The reason is, that the statements already follow from a two-level model with basic ingredients closed shell system (i.e. no magnetism), time-reversal symmetry, inversion

symmetry and the fact, that the HOMO- and LUMO-orbitals are conjugated, coupling well in similar ways to both leads.

Due to the large, interference induced slope of $T(E)$ in the valley region, one could expect to observe very large conductance fluctuations in the experiments – despite of the high molecular symmetry of C_{60} – due to weak environmental capacitive couplings. Our study would also suggest that the Seebeck coefficient does not exhibit such strong fluctuations because its dependency on the level alignment in the valley region is relatively weak, see e.g. Fig. 5 center. Both qualitative features are indeed observed in Ref. 25. On a quantitative level, we observe that the theoretical estimate for the Seebeck-coefficient overshoots the experimental one roughly by a factor of 2-4.

V. CONCLUSIONS

We have presented a detailed study of charge transport properties of the C_{60} -molecule coupled to Au-electrodes. Our main finding is that the electrical conductance of the molecule is strongly suppressed due to two interfering transmission channels. The phenomenon was interpreted as a precursor to a Fano-anti-resonance. This result has been established by combining ab-initio transport calculations with a toy-model analysis. This analysis also suggests, that a thermally driven current is significantly less sensitive to such interference effects due to cancellation effects in the transmission function and the Seebeck coefficient.

Acknowledgements

Support by the CFN and SPP 1243 are gratefully acknowledged. Also, LV thanks the Packard Foundation for support.

Appendix A: Coefficients for the Grimme correction

We employ the Grimme empirical correction (Eq. A1, A2 and A3)⁵⁰ to the total GGA energy in order to take van-der-Waals interactions into account. The coefficients that we used are given in Table III. For C and Cu-atoms, the values for C_6 and R_0 have been taken from Ref. 50. For gold atoms, the R_0 coefficient has been obtained from the radius of the electron density contour of a single gold atom and the C_6 coefficient has been obtained from a fit to data obtained from second order Moller-Plesset perturbation theory (MP2)⁵¹. Following Grimme⁵⁰ we used $d = 20$ and $s_6 = 1.05$.

$$E_{\text{disp}} = -s_6 \sum_{i=1}^{N_{\text{at}}-1} \sum_{j=i+1}^{N_{\text{at}}} \frac{C_6^{ij}}{R_{ij}^6} f_{\text{dmp}}(R_{ij}) \quad (\text{A1})$$

$$f_{\text{dmp}}(R_{ij}) = \frac{1}{1 + e^{-d(R_{ij}/R_0 - 1)}} \quad (\text{A2})$$

$$C_6^{ij} = \sqrt{C_6^i C_6^j} \quad (\text{A3})$$

	C_6 [J.nm ⁶ .mol ⁻¹]	R_0 [Å]
C	1.75	1.32
Cu	10.8	1.42
Au	21.9	1.58

TABLE III: Coefficients used for Grimme empirical correction.

Appendix B: Transport code

A detailed description of our transport simulations has been given in Ref. 29. We present a brief summary of the main steps. The effective Kohn-Sham (KS) Hamiltonian H_{KS} of the extended molecule is constructed from the KS-orbitals and energies previously computed by DFT (employing the TURBOMOLE package³⁴ in our case). The Green's function of the extended molecule is built from this Hamiltonian H_{KS}

$$G(E) = \frac{1}{E - H_{\text{KS}} - \Sigma} \quad (\text{B1})$$

where Σ is the self-energy of the reservoirs. It can be taken in the form²⁹

$$\Sigma_{nm} = \begin{cases} \delta_{nm}(\delta\epsilon - i\eta) & m, n \in S \\ 0 & m, n \notin S \end{cases} \quad (\text{B2})$$

This self-energy is diagonal in the atomic basis and has non-zero values only in the subspace S associated to the outermost atomic layer of each electrode. The parameter $\eta = 2.72$ eV is the leakage parameter. It is adjusted such a way that the transmission functions are (approximately) invariant under variation of η . The energy shift $\delta\epsilon$ is tuned for each calculation so that the Fermi level for the entire system remains unchanged compared to what has been obtained from DFT calculation, i.e. about the Fermi energy of the metal used for the electrodes. Here, we used $-1.25\text{eV} < \delta\epsilon < -1.15\text{eV}$ for Au and $-2.00\text{eV} < \delta\epsilon < -1.94\text{eV}$ for Cu.

The local density of states (LDOS) projected on the molecule can then be written

$$\text{LDOS}(E) = -\frac{1}{\pi} \sum_{n \in M} \Im G_{nn} \quad (\text{B3})$$

where M is the subspace associated to the atoms of the molecule.

The transmission function is given by the following version of the Landauer formula⁵²

$$T(E) = \text{Tr} \{ \Gamma_L G \Gamma_R G^\dagger \} \quad (\text{B4})$$

with $\Gamma_{L,R}$ defined by

$$\Gamma_{L,R} = i(\Sigma_{L,R} - \Sigma_{L,R}^\dagger). \quad (\text{B5})$$

Appendix C: LDOS projected on molecular orbitals

In order to illustrate more clearly the mixing of molecular states, we here introduce a projection of the LDOS on specific ‘‘coupled molecular orbitals’’, $|\mu\rangle$. The formal definition of such orbitals is given by the following construction. Again, we construct the KS-Hamiltonian H_{KS} from the KS-orbitals and energies of the DFT-calculation that has been done for the extended molecule (C_{60} plus parts of the leads). In the orthogonalized atomic basis set one can partition H_{KS} in the following way,

$$H_{\text{KS}} = \begin{pmatrix} H_L & V_{LC} & V_{LR} \\ V_{LC}^* & H_C & V_{RC} \\ V_{LR}^* & V_{RC}^* & H_R \end{pmatrix}. \quad (\text{C1})$$

where as usual L, R refer to the Hilbert spaces of the left and right electrode and C comprises the remaining part of the full Hilbert space that belongs to the molecule. The states $|\mu\rangle$ are the eigenvectors of the central block H_C . They are related to the molecular states of C_{60} in vacuum, but some effects of the electrode coupling are taken into account. Since the states $|\mu\rangle$ form a complete basis of the molecular Hilbert-subspace corresponding to H_C , the LDOS on the molecule can then be decomposed into the contributions of each molecular orbital

$$\text{LDOS}(E) = -\frac{1}{\pi} \sum_{\mu} \langle \mu | \Im G(E) | \mu \rangle. \quad (\text{C2})$$

The LDOS projected on a molecular orbital $|\mu\rangle$ can then be identified as $-\frac{1}{\pi} \langle \mu | \Im G(E) | \mu \rangle$.

The local density of states projected on the two relevant molecular orbitals is depicted in Fig. 8. It shows that in the valley region of the transmission between HOMO- and LUMO-resonances two associated orbitals contribute similarly to the LDOS. This suggests that there is a possibility for these orbitals to give interfering terms in the transmission function $T(E)$.

Appendix D: Two level (toy) model

We recall properties of the two-state (toy) model that accounts for the transport characteristics of non-interacting quantum dots with two effective transport levels. As opposed to earlier work⁵³, we investigate the model analytically in its full parameter space.

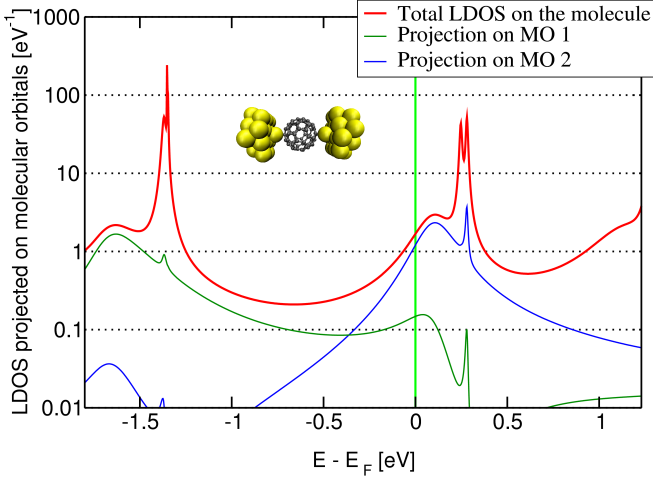


FIG. 8: (Color) Local density of states projected on the two strongly coupled molecular orbitals (MO 1 and MO 2) for the geometry where the adatom sits on-top of a C-atom.

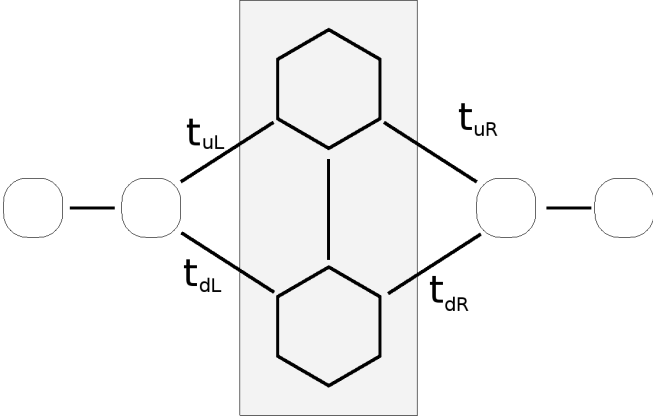


FIG. 9: Schematic representation of the two-level model with the inner part representing the Hamiltonian H (grey shaded) and the couplings to the leads.

1. Definition

Quite generally, the transmission is given by a formula of the Landauer type (B4), $T(E) = \text{Tr} \{ \Gamma_L G \Gamma_R G^\dagger \}$. For toy model $\Gamma_{L,R}$ and G are 2×2 -matrices. We have for the inverse Green's function

$$G^{-1}(E) = E - H - \Sigma(E) \quad (\text{D1})$$

where H is a non-interacting two-level Hamiltonian and $\Sigma(E)$ denotes the self-energy that describes the coupling to a left and right single channel wire: $\Sigma = \Sigma_R + \Sigma_L$. This

self energy has the general structure

$$\begin{aligned} \Sigma_\alpha(E) &= g_\alpha(E) \begin{pmatrix} |t_{u\alpha}|^2 & t_{u\alpha}^* t_{d\alpha} \\ t_{d\alpha}^* t_{u\alpha} & |t_{d\alpha}|^2 \end{pmatrix} \quad (\text{D2}) \\ &= \begin{pmatrix} t_{u\alpha}^* \\ t_{d\alpha}^* \end{pmatrix} g_\alpha(E) (t_{u\alpha}, t_{d\alpha}), \quad \alpha=L,R \end{aligned} \quad (\text{D3})$$

where $t_{u\alpha}, t_{d\alpha}$ denote the hybridization matrix elements that connect the two level, up and down, with the wire reservoirs; $g_\alpha(E)$ resembles a scalar, complex valued function, the "surface Greensfunction" of each wire at the point contacting to the two-level system. We have

$$\Gamma_\alpha = -i (\Sigma_\alpha(E) - \Sigma_\alpha^\dagger(E)); \quad (\text{D4})$$

Interference effects can occur, if $\Gamma_{L,R}$ and G do not commute, so that they cannot be diagonalized simultaneously. In order to highlight them, we begin substituting (D3) into the trace formula; we obtain

$$T(E) = (2\pi)^2 \varrho_L \varrho_R \left| (t_{uL} t_{dL}) G \begin{pmatrix} t_{uR}^* \\ t_{dR}^* \end{pmatrix} \right|^2. \quad (\text{D5})$$

with the contact density of states $\varrho(E) = \frac{-1}{\pi} \Im g_\alpha(E)$. Next, we rotate into the basis of eigenfunctions of $G(E)$

$$G(E) = U \begin{pmatrix} \frac{1}{E-z_0} & 0 \\ 0 & \frac{1}{E-z_1} \end{pmatrix} U^{-1} \quad (\text{D6})$$

In general, the pole positions $z_{0,1}$ and the eigenvectors comprising the columns of the rotation matrix U inherit a dependency on energy, E , through $\Sigma(E)$. In order to simplify notation we introduce effective hybridization matrix elements, v

$$(v_{0L}, v_{1L}) = \sqrt{2\pi \varrho_\alpha} (t_{uL} t_{dL}) U \quad (\text{D7})$$

$$\begin{pmatrix} v_{0R}^* \\ v_{1R}^* \end{pmatrix} = \sqrt{2\pi \varrho_\alpha} U^{-1} \begin{pmatrix} t_{uR}^* \\ t_{dR}^* \end{pmatrix} \quad (\text{D8})$$

and transmission coefficients

$$\begin{aligned} \tau_{\alpha\beta}(E) &= 2\pi \sqrt{\varrho_\alpha \varrho_\beta} (t_{u\alpha} t_{d\alpha}) G \begin{pmatrix} t_{u\beta}^* \\ t_{d\beta}^* \end{pmatrix} \\ &= \frac{v_{0\alpha} v_{0\beta}^*}{E - z_0} + \frac{v_{1\alpha} v_{1\beta}^*}{E - z_1} \end{aligned} \quad (\text{D9})$$

that allow us to write

$$T(E) = |\tau_{LR}(E)|^2 \quad (\text{D10})$$

To explicitly single out the interference term, we employ a decomposition

$$T(E) = T_0(E) + T_1(E) + T_{01}(E). \quad (\text{D11})$$

The two first terms constitute the non-mixing contributions from each energy level

$$T_0(E) = \frac{|v_{0L}|^2 |v_{0R}|^2}{|E - z_0|^2}, \quad T_1(E) = \frac{|v_{1L}|^2 |v_{1R}|^2}{|E - z_1|^2} \quad (\text{D12})$$

Each term refers to a single pole only and thus is reproduced by the model of isolated resonances, Eq. (2). Interference enters via the mixed term

$$T_{01}(E) = 2\sqrt{T_0 T_1} \cos(\Psi_c - \Theta) \quad (\text{D13})$$

$$\Psi_c = \arg(v_{0L} v_{0R}^* v_{1L} v_{1R}) \quad (\text{D14})$$

$$\Theta(E) = \arg((E - z_0)(E - z_1^*)) \quad (\text{D15})$$

As is seen from equation (D13), interference effects are controlled by two angles, Ψ_c and Θ . They exhibit quite different generic properties. Ψ_c carries an energy dependency only via $\Sigma(E)$ that reflects a dispersion in the (local) density of states in the reservoirs. Because the latter often is very smooth compared to the level splitting, $|\epsilon_0 - \epsilon_1|$ with $\Re z_i = \epsilon_i$, it can typically be ignored, so that for practical purposes Ψ_c is energy independent. By contrast, $\Theta(E)$ can exhibit a very sharp energy dependency, especially in the limit of low damping.

Remark: Level broadening

To reveal further transport properties of the two-level transmission function, we relate the amplitudes $|v_{0\alpha}|^2$ to the level broadenings γ_i . This broadening originates from the anti-hermitian part of the inverse Green's function

$$G^{-1} = G_0^{-1} + \frac{1}{2i}\Gamma \quad (\text{D16})$$

$$G_0^{-1} = E - H - \frac{1}{2}(\Sigma + \Sigma^\dagger). \quad (\text{D17})$$

We have

$$\text{Tr} G^{-1} = 2E - z_0 - z_1 = \text{Tr} G_0^{-1} + \frac{1}{2i}\text{Tr} \Gamma. \quad (\text{D18})$$

Since G_0^{-1}, Γ by construction are hermitian, each trace is real; hence

$$\Re[z_0 + z_1] = \text{Tr} \left[H + \frac{1}{2}(\Sigma + \Sigma^\dagger) \right] \quad (\text{D19})$$

$$\Im[z_0 + z_1] = \frac{1}{2}\text{Tr} \Gamma. \quad (\text{D20})$$

The second line simplifies after recalling (D3):

$$\Im[z_0 + z_1] = \frac{1}{2} \left(-2\pi \sum_{\alpha} \rho_{\alpha} (|t_{u\alpha}|^2 + |t_{d\alpha}|^2) \right) \quad (\text{D21})$$

$$= -\frac{1}{2} \sum_{\alpha} |v_{0\alpha}|^2 + |v_{1\alpha}|^2 \quad (\text{D22})$$

Remark: Unitarity theorem

We split the transmission coefficients into hermitian and anti-hermitian contributions:

$$\begin{aligned} \tau_{\alpha\beta} &= 2\pi\sqrt{\varrho_{\alpha}\varrho_{\beta}}(t_{u\alpha}t_{d\alpha})G \begin{pmatrix} t_{u\beta}^* \\ t_{d\beta}^* \end{pmatrix} \\ &= 2\pi\sqrt{\varrho_{\alpha}\varrho_{\beta}}(t_{u\alpha}t_{d\alpha}) \left[\frac{1}{2}(G+G^\dagger) + \frac{i}{2}G\Gamma G^\dagger \right] \begin{pmatrix} t_{u\beta}^* \\ t_{d\beta}^* \end{pmatrix}. \end{aligned}$$

The first term simplifies to $\frac{1}{2}[\tau_{\alpha\beta} + \tau_{\beta\alpha}^*]$ while the second one takes the form

$$\begin{aligned} &\frac{(2\pi)^2}{2i}\sqrt{\varrho_{\alpha}\varrho_{\beta}}(t_{u\alpha}t_{d\alpha}) \cdot \\ &\quad \cdot G \left[\sum_{\bar{\alpha}} \varrho_{\bar{\alpha}} \begin{pmatrix} t_{u\bar{\alpha}}^* \\ t_{d\bar{\alpha}}^* \end{pmatrix} (t_{u\bar{\alpha}}t_{d\bar{\alpha}}) \right] G^\dagger \begin{pmatrix} t_{u\beta}^* \\ t_{d\beta}^* \end{pmatrix} \\ &= \frac{1}{2i} \sum_{\bar{\alpha}} \tau_{\alpha\bar{\alpha}} \tau_{\beta\bar{\alpha}}^* \quad (\text{D23}) \end{aligned}$$

Summarizing, we have in a matrix notation the general statement

$$\tau - \tau^\dagger = -i\tau\tau^\dagger \quad (\text{D24})$$

that satisfies a unitarity theorem $\tau^{-1} - [\tau^\dagger]^{-1} = i$.

2. Time reversal symmetry

In the presence of time reversal symmetry the matrices G_0^{-1} and Γ are both real symmetric, so G^{-1} is (complex) symmetric and U is (complex) orthogonal. Then simplifications arise for T_{01} .

We focus the discussion on the weak coupling limit, where the resonance positions are split by an amount that considerably exceeds their broadening, $|\epsilon_1 - \epsilon_0| \gg \gamma_{0,1}$. In this case we can consider the anti-hermitian piece of the self energy $\frac{-i}{2}\Gamma$ as a perturbation and the eigenvectors \mathbf{u}_i are real to first order in γ_i ; at least to this order U is real orthogonal. Hence, also the effective hybridization matrix elements $v_{i\alpha}$ are real and therefore Ψ_c takes values zero or π ; we have

$$\cos(\Psi_c - \Theta(E)) = \text{sign}(v_{0L}v_{0R}v_{1L}v_{1R}) \cos \Theta(E) \quad (\text{D25})$$

To the leading order in γ_i the energy dependency is described by

$$\cos \Theta(E) = \text{sign}([E - \epsilon_0][E - \epsilon_1]). \quad (\text{D26})$$

Equations (D25, D26) are important because they highlight two characteristic features of the interference term T_{01} . First, whether constructive ($\cos(\Psi_c - \Theta) > 0$) or destructive ($\cos(\Psi_c - \Theta) < 0$) interference prevails in the intermediate range $\epsilon_0 < E < \epsilon_1$ is controlled by the model dependent first factor in (D25). If it is positive,

$\Psi_c = 0$, interference is destructive; it is constructive in the alternative case $\Psi_c = \pi$.

Second, T_{01} has a very sharp dependency on energy when E sweeps by ϵ_0 or ϵ_1 . In fact, the corresponding derivative diverges in the limit $\gamma_i \rightarrow 0$; specifically, with Eq. (D15) we have

$$\cos \Theta(E) = \frac{(E - \epsilon_0)(E - \epsilon_1) + \gamma_0 \gamma_1}{|E - z_0||E - z_1|} \quad (\text{D27})$$

$$\sin \Theta(E) = \frac{\gamma_1(E - \epsilon_0) + \gamma_0(E - \epsilon_1)}{|E - z_0||E - z_1|} \quad (\text{D28})$$

3. Limiting cases: symmetric vs asymmetric lead couplings

We now analyze two limiting cases in which the angle Ψ_c is either close to π (constructive interference) or close to zero (destructive interference).

a. Fully symmetric coupling: Fano anti-resonance

We begin with the second situation, destructive interference, which is the easier one to investigate and exploit Eq. (D24) now for a system with completely symmetric coupling, $t_{uL} = t_{uR} = t_u$, $t_{dL} = t_{dR} = t_d$. This situation is realized, e.g., to a very good approximation for cross-conjugated molecular wires with side coupling chains as investigated in Ref. [54]. A cross-conjugated molecule was studied recently experimentally in Ref. [55], where the Fano-antiresonance has indeed been observed.

Our interest is in the off-diagonal matrix element,

$$\tau_{\text{LR}}(E) = \Re[\tau_{\text{LR}}(E)] - \frac{i}{2} \frac{(\rho_L + \rho_R)}{\sqrt{\varrho_L \varrho_R}} |\tau_{\text{LR}}(E)|^2 \quad (\text{D29})$$

This equation implies the following fact: Let E^* be a root of the real part of the transmission coefficients, $\Re[\tau_{\text{LR}}(E^*)] = 0$. Then, at this energy also the imaginary piece has a vanishing physical solution: $\Im[\tau_{\text{LR}}(E^*)] = 0$.

For generic situations E^* can be shown to be real, so that there is no transmission at this energy, $T(E^*) = 0$. Namely, let $\tilde{U}(E)$ be the unitary rotation diagonalizing the hermitian matrix $G + G^\dagger$; then

$$\Re[\tau_{\text{LR}}(E)] = 2\pi\sqrt{\rho_L \rho_R} \left[\frac{|\tilde{v}_0|^2}{E - \tilde{\epsilon}_0} + \frac{|\tilde{v}_1|^2}{E - \tilde{\epsilon}_1} \right] \quad (\text{D30})$$

where $\tilde{\epsilon}_{0,1}$ denote the real eigenvalues of $(G + G^\dagger)/2$ and $(\tilde{v}_0, \tilde{v}_1) = (t_u, t_d)\tilde{U}(E)$. Under the assumption, that the

energy dependency of the eigenvalues is weak (i.e. in the wide band limit, where $\varrho_\alpha(E)$ is nearly constant), Eq. (D30) has the real numbered root

$$E^* = \frac{\tilde{\epsilon}_0 |\tilde{v}_1|^2 + \tilde{\epsilon}_1 |\tilde{v}_0|^2}{|\tilde{v}_0|^2 + |\tilde{v}_1|^2}. \quad (\text{D31})$$

It constitutes a weighed average that is situated between the two pole positions.

Since at E^* we have complete destructive interference, it is clear that at this energy $\Psi_c - \Theta(E^*) = \pi$. Since in the valley region Θ is close to π we have $\Phi_c \approx 0$ with corrections in $\gamma_{0,1}$. Therefore, in the valley region away from the anti-resonance E^* we expect

$$T_{01} = 2\sqrt{T_0 T_1} \cos \Theta(E) \quad (\text{D32})$$

with $\cos \Theta(E)$ as given in Eq. (D27).

b. Fully asymmetric coupling

The previous example suggests, that constructive interference could be expected for an asymmetric limit, $t_{uR}, t_{dL} = 0$. In this case, because of equations (D7,D8) the effective hybridization matrix elements reproduce the entries of U and U^{-1} :

$$\begin{aligned} v_{iL} &= \sqrt{2\pi\varrho_L} t_{uL} U_{0i} \\ v_{iR}^* &= \sqrt{2\pi\varrho_R} t_{dR}^* [U^{-1}]_{i1} \end{aligned}$$

so that

$$\Psi_c = \arg(U_{00}[U^{-1}]_{01}[U^{-1}]_{11}^* U_{01}^*) \quad (\text{D33})$$

The product in brackets is easy to evaluate in the presence of time reversal symmetry recalling that U is orthogonal in this case. Like any orthogonal 2×2 -rotation matrix it has a representation

$$U = \begin{pmatrix} \cos w & \sin w \\ -\sin w & \cos w \end{pmatrix}, \quad w \in \mathbb{C}$$

We obtain $\Psi_c = \pi$. Hence, we now expect a constructive interference contribution

$$T_{01} = -2\sqrt{T_0 T_1} \cos \Theta(E). \quad (\text{D34})$$

where again $\cos \Theta(E)$ is given in Eq. (D27).

¹ X. Lu, M. Grobis, K. H. Khoo, S. G. Louie, and M. F. Crommie, Phys. Rev. Lett. **90**, 096802 (2003), URL <http://link.aps.org/doi/10.1103/PhysRevLett.90.096802>.

² X. Lu, M. Grobis, K. H. Khoo, S. G. Louie, and M. F. Crommie, Phys. Rev. B **70**, 115418 (2004).

³ C. Rogero, J. I. Pascual, J. Gómez-Herrero, and A. M.

- Baró, J. Chem. Phys. **116**, 832 (2002).
- ⁴ J. D. Sau, J. B. Neaton, H. J. Choi, S. G. Louie, and M. L. Cohen, Phys. Rev. Lett. **101**, 026804 (2008), URL <http://link.aps.org/doi/10.1103/PhysRevLett.101.026804>.
 - ⁵ I. F. Torrente, K. J. Franke, and J. I. Pascual, J. Phys.: Condens. Matter **20**, 184001 (2008).
 - ⁶ A. Tamai, A. P. Seitsonen, F. Baumberger, M. Hengsberger, Z.-X. Shen, T. Greber, and J. Osterwalder, Phys. Rev. B **77**, 075134 (2008).
 - ⁷ E. Abad, C. Ganzalez, J. Ortega, and F. Flores, Organic Electronics **11**, 332 (2010).
 - ⁸ I. Hamada and M. Tsukada, Phys. Rev. B **83**, 245437 (2011), URL <http://link.aps.org/doi/10.1103/PhysRevB.83.245437>.
 - ⁹ H. Park, J. Park, A. K. L. Lim, E. H. Anderson, A. P. Alivisatos, and P. L. McEuen, Nature **407**, 57 (2000).
 - ¹⁰ L. H. Yu and D. Natelson, Nano Letters **4**, 79 (2004).
 - ¹¹ A. N. Pasupathy, R. C. Bialczak, J. Martinek, J. E. Grose, L. A. K. Donev, P. L. McEuen, and D. C. Ralph, Science **306**, 86 (2004).
 - ¹² J. J. Parks, A. R. Champagne, G. R. Hutchison, S. Flores-Torres, H. D. Abruna, and D. C. Ralph, Phys. Rev. Lett. **99**, 026601 (2007).
 - ¹³ N. Roch, S. Florens, V. Bouchiat, W. Wernsdorfer, and F. Balestro, Nature **453**, 633 (2008).
 - ¹⁴ G. Schulze, K. J. Franke, and J. I. P. and, New J. of Phys. **10**, 065005 (2008).
 - ¹⁵ G. Schulze, K. J. Franke, A. Gagliardi, G. Romano, C. S. Lin, A. L. Rosa, T. A. Niehaus, and T. Frauenheim, Phys. Rev. Lett. **100**, 136801 (2008).
 - ¹⁶ T. Frederiksen, K. J. Franke, A. Arnau, G. Schulze, J. I. Pascual, and N. Lorente, Phys. Rev. B **78**, 233401 (2008).
 - ¹⁷ A. Gagliardi, G. Romano, A. Pecchia, A. D. Carlo, T. Frauenheim, and T. A. Nienhaus, New Journal of Physics **10**, 065020 (2008).
 - ¹⁸ J. Fock, J. K. Sorensen, E. Lortscher, T. Vosch, C. A. Martin, H. Riel, K. Kilsa, T. Bjornholm, and H. van der Zant, Phys. Chem. Chem. Phys. **13**, 14325 (2011), URL <http://dx.doi.org/10.1039/C1CP20861F>.
 - ¹⁹ N. Néel, J. Kröger, L. Limot, T. Frederiksen, M. Brandbyge, and R. Berndt, Phys. Rev. Lett. **98**, 065502 (2007).
 - ²⁰ G. Schull, T. Frederiksen, M. Brandbyge, and R. Berndt, Phys. Rev. Lett. **103**, 206803 (2009).
 - ²¹ G. Schull, T. Frederiksen, A. Arnau, D. Sanchez-Portal, and R. Berndt, Nature Nanotechnology **6**, 23 (2010).
 - ²² G. Schull, Y. J. Dappe, C. Gonzalez, H. Bulou, and R. Berndt, Nano Letters **11**, 3142 (2011).
 - ²³ T. Böhler, A. Edtbauer, and E. Scheer, Phys. Rev. B **76**, 125432 (2007), URL <http://link.aps.org/doi/10.1103/PhysRevB.76.125432>.
 - ²⁴ M. Kiguchi and K. Murakoshi, J. Phys. Chem. C **112**, 8140 (2008).
 - ²⁵ S. K. Yee, J. A. Malen, A. Majumdar, and R. A. Segalman, Nano Letters **11**, 4089 (2011).
 - ²⁶ M. Mayor, H. B. Weber, J. Reichert, M. Elbing, C. von Hanch, D. Beckmann, and M. Fischer, Angewandte Chemie-International Edition **2003**, 5834 (2003).
 - ²⁷ C. A. Martin, D. Ding, J. K. Sorensen, T. Bjornholm, J. van Ruitenbeek, and H. S. J. van der Zant, J. Am. Chem. Soc. **130**, 13198 (2008).
 - ²⁸ E. Leary, M. T. Gonzalez, C. van der Pol, M. R. Bryce, S. Filippone, N. Martin, G. Rubio-Bollinger, and N. Agrait, Nano Letters **11**, 2236 (2011).
 - ²⁹ A. Arnold, F. Weigend, and F. Evers, Journal of Chemical Physics **126**, 174101 (2007).
 - ³⁰ M. K. Shukla, M. Dubey, and Leszczynski, ACS Nano **2**, 227 (2008).
 - ³¹ M. K. Shukla, M. Dubey, E. Zakar, and J. Leszczynski, J. Phys. Chem. **113**, 11351 (2009).
 - ³² S. Bilan, L. A. Zotti, F. Pauly, and J. C. Cuevas, arXiv:1203.3101v1 (2012).
 - ³³ T. Ono and K. Hirose, Phys. Rev. Lett. **98**, 026804 (2007).
 - ³⁴ R. Ahlrichs, M. Bär, M. Häser, H. Horn, and C. Kölmel, Chem. Phys. Lett. **162**, 165 (1989).
 - ³⁵ A. Becke, Phys. Rev. A **38**, 3098 (1988).
 - ³⁶ S. Grimme, Journal of Computational Chemistry **25**, 1463 (2004).
 - ³⁷ S. T. Schneebeli, M. Kamenetska, Z. Cheng, R. Skouta, R. A. Friesner, L. Venkataraman, and R. Breslow, J. Am. Soc. Chem. **133**, 2136 (2011).
 - ³⁸ R. W. Lof, M. A. van Veenendaal, B. Koopmans, H. T. Jonkman, and G. A. Sawatzky, Phys. Rev. Lett. **68**, 3924 (1992).
 - ³⁹ U. Sivan and Y. Imry, Phys. Rev. B **33**, 551 (1986), URL <http://link.aps.org/doi/10.1103/PhysRevB.33.551>.
 - ⁴⁰ S. H. Ke, M. Yang, S. Cortarolo, and H. U. Baranger, Nano Lett. **9**, 1011 (2009).
 - ⁴¹ J. R. Widawsky, P. Darancet, J. B. Neaton, and L. Venkataraman, Nano Lett. **354**, 12 (2012).
 - ⁴² M. Paulsson and S. Datta, Phys. Rev. B **67**, 241403 (2003), URL <http://link.aps.org/doi/10.1103/PhysRevB.67.241403>.
 - ⁴³ D. Segal, Phys. Rev. B **72**, 165426 (2005), URL <http://link.aps.org/doi/10.1103/PhysRevB.72.165426>.
 - ⁴⁴ S.-H. Ke, W. Yang, and H. U. Baranger, Nano Lett. **8**, 3257 (2008).
 - ⁴⁵ D. M. Cardamone, C. A. Stafford, and S. Mazumdar, Nano Lett. **6**, 2423 (2006).
 - ⁴⁶ J. P. Bergfield, Z.-F. Liu, K. Burke, and C. A. Stafford, Phys. Rev. Lett. **108**, 066801 (2012).
 - ⁴⁷ G. Stefanucci and S. Kurth, Phys. Rev. Lett. **107**, 216401 (2011).
 - ⁴⁸ P. Schmitteckert and F. Evers, Phys. Chem. Chem. Phys. **13**, 14417 (2011).
 - ⁴⁹ P. Schmitteckert and F. Evers, Phys. Rev. Lett. **100**, 086401 (2008).
 - ⁵⁰ S. Grimme, Journal of Computational Chemistry **27**, 1787 (2006).
 - ⁵¹ M. Peter, Master's thesis, Universität Karlsruhe (2009).
 - ⁵² Y. Meir and N. Wingreen, Phys. Rev. Lett. **68**, 2512 (1992).
 - ⁵³ G. C. Solomon, D. Q. Andrews, T. Hansen, R. H. Goldsmith, M. R. Wasielewski, R. P. Van Duyne, and M. A. Ratner, J. Chem. Phys. **129**, 054701 (2008).
 - ⁵⁴ G. C. Solomon, D. Q. Andrews, R. H. Goldsmith, T. Hansen, M. R. Wasielewski, R. P. Van Duyne, and M. A. Ratner, J. Chem. Phys. **130**, 17301 (2008).
 - ⁵⁵ C. M. Guedon, H. Valkenier, T. Markussen, K. S. Thygesen, J. C. Hummelen, and S. J. van der Molen, Nat. Nano. **7**, 305 (2012).
 - ⁵⁶ Here, we use a slightly simplified version in which we choose an approximation $\Psi_c = 0, \pi$. In this way we eliminate two fitting parameters, the real angle Ψ_c and a background contribution that cuts off the Fano-anti-resonance. Both parameters need to be accounted for if the simplified (toy) model, when adjusted near the resonance positions, does not capture the behavior of the transmission function in the valley region.